

Probing Majorana modes via local spin dynamics

Johannes Bjerlin ^{1,2,3,*} Anders S. Sørensen,¹ and Stephan Haas²

¹*Niels Bohr Institute, University of Copenhagen, Blegdamsvej 17, Copenhagen DK-2100, Denmark*

²*Department of Physics and Astronomy, University of Southern California, Los Angeles, California 90089-0484, USA*

³*Mathematical Physics, Lund University, SE-22100 Lund, Sweden*



(Received 14 February 2022; revised 8 June 2022; accepted 8 June 2022; published 14 July 2022)

We investigate Majorana modes in a quantum spin chain with bond-dependent exchange interactions by studying its dynamics. Specifically, we consider two-time correlations for the anisotropic Kitaev-Heisenberg (KH) Hamiltonian close to the so-called Kitaev critical point. Here the model coincides with a phase boundary of two uncoupled instances of Kitaev's model for p -wave superconductors, together supporting a degenerate ground state characterized by multiple Majorana modes. In this regime, the real-time dynamics of local spins reveal a set of *strong zero modes*, corresponding to a set of protruding frequencies in the two-time correlation function. We derive perturbative interactions that map the KH spin chain onto the topological regime of Kitaev's fermionic model, thus opening up a bulk gap while retaining almost degenerate modes in the mesoscopic regime, i.e., for finite system sizes. This showcases the emergence of Majorana modes in a chain of effective dimers. Here, the binding energy within each unit cell competes with the interdimer coupling to generate a finite-size energy gap, in analogy with local energy terms in the transverse-field Ising model. These modes give rise to long coherence times of local spins located at the system edges. By breaking the local symmetry in each dimer, one can also observe a second class of Majorana modes in terms of a beating frequency in the two-time correlations function of the edge spin. Furthermore, we develop a scenario for realizing these model predictions in ion-trap quantum simulators with collective addressing of the ions.

DOI: [10.1103/PhysRevB.106.035414](https://doi.org/10.1103/PhysRevB.106.035414)

I. INTRODUCTION

Topological modes are ubiquitous in many-body (MB) models, but their experimental detection and control in naturally occurring quantum systems can be challenging [1]. A prominent example is the Majorana fermion (MF), a non-Abelian anyon with nontrivial exchange statistics [2], which has been studied for a wide range of MB systems [3]. The perhaps simplest manifestation of an MF was proposed by Kitaev, who introduced a toy model for a fermionic quantum wire in the form of a one-dimensional (1D) p -wave paired superconductor [4]. The microscopic origin of this model was worked out for d^5 transition metals [5], and it is up until this day an important tool in the active pursuit of controllable MFs [6]. Kitaev's fermionic model is intimately connected to the Ising [7] and Kitaev-Heisenberg (KH) spin models. While the Ising model is ubiquitous and studied extensively in many contexts the KH model, with a potential realization in $4d^5$ ruthenium trichloride α -RuCl₃ [8,9], is less commonplace. The KH model attains frustration due to bond-dependent

exchange couplings, and it may support long-range magnetic order [10,11] and quantum spin-liquid states (SQLs) [9,12–14]. The scope of this paper is to analyze the emergence of MFs from the perspective of few-to-many body physics. In this field, recent advances in computational and experimental techniques (particularly within ultracold atomic gases [15,16]), has sparked experimental studies of, e.g., few-body magnetism without a lattice in one dimension [17], the formation of a Fermi sea [18] and, more recently, a few-body analog of a quantum phase transition in two dimensions [19,20]. The advancements mentioned above highlight the growing interest in the controlled simulation of mesoscopic systems and number-conserving models with exotic features, which can shed light on the origins of quantum MB phases. Already, several studies have been conducted on MFs and topological phases in number conserving lattice models, motivated by the quest for a topological quantum computer [21]. This includes numerical studies of the topological features themselves, using density matrix renormalization group techniques [6,22,23], as well as studies focusing on the microscopic origins and possible realizations of the models in which they arise [22,24–27]. This also extends to studies of dynamical observables [26,28,29], and in a recent preprint some of the few-body aspects of Majorana quasiparticles were laid out [30], underlining the promise of quantum simulation of few-body physics as a way to study complex MB phenomena using a bottom-up approach.

We here aim to study the emergence of an MF from dynamical observables in a quantum simulation of a 1D KH

*Johannes.Bjerlin@matfys.lth.se

few-body spin model. For large-scale calculations of topological modes (and SQLs), the use of quantum simulation with engineered lattice Hamiltonians in cold atom systems has been a viable pathway [31,32]. However, these systems typically require extremely low temperatures. A favorable alternative is given by simulators based on trapped ions [33–35]. Such setups are versatile and can function at comparatively high temperatures [36]. Recent successful examples of ion-trap simulations include a dynamical phase transition for a 53-qubits system [25], as well as quasiparticle dynamics in an Ising spin chain [37]. While quantum simulation promises remarkable speed up in the characterization of complex systems [38], so far most implementations have focused on well-studied static properties for which other highly effective numerical and analytical tools are available. While there have been some advancements in classical computation of time-dependent observables [39] they are typically costly [40,41]. There is to this date no general method to efficiently simulate the dynamics of large and strongly correlated systems. Quantum simulation of dynamical features is hence especially compelling [28,42]. Recent examples of dynamical quantum simulation include studies of two-time correlations (TTCs) [43–45] and out-of-time correlations (OTOCs) [46,47] in interacting models, which have provided a new understanding of phase transitions and MB modes. The Ising model has been probed using the real-time dynamics of a single spin [48]. This type of dynamical observable is especially relevant for our setup and has already been utilized for a range of open boundary models where it is clear that spins may exhibit long coherence times owing to the presence of strong zero modes [29,49,50]. Similarly, in fermionic models topological Majoranas have been studied via survival rates of edge modes [51] and via Leggett-Garg inequalities [44]. These techniques are powerful since they can be used at high temperatures [42,50,52].

Here we focus on few-body phases of an interacting 1D quantum spin model (SM) that emulates Majorana edge modes (MEMs), investigating its dynamical features in the few-to-many body limit. The term “emulate” refers to the fact that the MEMs are topologically nontrivial only in the fermionic representation of the model [7]. Interestingly, the dynamical features of the SM still manifest a large discrepancy between bulk and edge. We begin by presenting an appropriate form of the (anisotropic) Kitaev-Heisenberg Hamiltonian [6], using two parameters to tune the system between different phases around one of its critical points. We briefly discuss the various relevant phases in the static regime before investigating their individual dynamical signatures in local spin observables, focusing on MEMs. We use two-time correlation (TTC) functions to probe the Majorana bulk gap as well as the interaction-induced energy splitting between edge modes. This detection protocol elucidates the few-to-many-body development of MEMs without the requirement of deterministic preparation of any particular quantum state. Finally, we discuss a possible experimental realization of these findings in an ion-trap setup.

The static properties of the Hamiltonian are studied by means of exact diagonalization, using the full basis set of \hat{S}_i^z eigenstates. We utilize a sparse representation of the

Hamiltonian and obtain the low-lying eigenvectors using the open-source library *Eigen* [53] developed for c++. For determining dynamical features, we numerically solve the time-dependent Schrödinger equation, using the fourth-order Runge-Kutta method for temporal discretization. Here the sparse matrix-vector multiplication can be easily parallelized and distributed over multiple cores. Using this setup, we can currently treat systems of up to chain lengths $L \sim 20$ on a single standard machine.

II. A TUNABLE MODEL FOR MAJORANA EDGE MODES

We focus on the 1D KH model describing an even number L of spin-1/2 subsystems interacting via nearest-neighbor (NN) couplings. The unit cells consist of two spins, where the interaction inside the unit cell is different from the interaction between neighboring unit cells. The interaction between the spins is described by the Hamiltonian

$$\begin{aligned} \hat{H}_{KH} &= K \sum_{j=1}^{L/2} (\hat{S}_{2j-1}^x \hat{S}_{2j}^x + \hat{S}_{2j}^y \hat{S}_{2j+1}^y) + J \sum_{i=1}^L (\hat{S}_i^x \hat{S}_{i+1}^x + \hat{S}_i^y \hat{S}_{i+1}^y) \\ &= \frac{2J + K}{4} \sum_{i=1}^L (\hat{S}_i^+ \hat{S}_{i+1}^- + \hat{S}_i^- \hat{S}_{i+1}^+) \\ &\quad + \frac{K}{4} \sum_{i=1}^L (-1)^i (\hat{S}_i^+ \hat{S}_{i+1}^+ + \hat{S}_i^- \hat{S}_{i+1}^-). \end{aligned} \quad (1)$$

Here j is the unit cell index, and i is the spin index. \hat{S}_i^x corresponds to a local operator of spin i , describing spin along the x axis. We further set $\hbar = 1$, so that $\hat{S}_i^D = 1/2 \cdot \sigma_i^D$ in terms of Pauli matrices σ_i^D . This quantum MB Hamiltonian, with tunable parameters J and K , can be considered an inhomogeneous and anisotropic Heisenberg XY model with exchange terms and additional sign-alternating double spin-flip interactions [6,54]. Similar models have been studied in the context of quantum phase transitions, criticality and magnetic long-range order [14,55,56]. We shall introduce perturbing terms \hat{V}_δ to this Hamiltonian, as to produce Majorana edge modes. The appropriate form of these perturbation will be derived later in this section. We, however, first parametrize the basic Hamiltonian in terms of a polar parameter, θ , governing the relative strength and signs of the interactions according to

$$K = \sin \theta, J = \cos \theta, \quad (2)$$

and we use $\sqrt{K^2 + J^2} = 1$ as the unit of energy throughout.

We begin by studying the phase diagram of the system close to the so-called *Kitaev points*, located at $\theta_{KP} = \pm\pi/2 \rightarrow K = \pm 1, J = 0$ and $\theta_{KP} = 5\pi/4 \pm \pi/2 \rightarrow K = \pm 1/\sqrt{2}, J = \mp 1/\sqrt{2}$. Applying the Jordan-Wigner transformation, we can find the corresponding fermionic model (see the Supplemental Materials [57] Sec. I). The fermionic Hamiltonian can be directly decomposed into a sum of two separate systems, A and B, of length $L/2$ so that

$$\hat{H}_{KH} = \frac{K + J}{4} \hat{H}_A + \frac{J}{4} \hat{H}_B,$$

with

$$\hat{H}_A = \frac{1}{2} \sum_{j=1} \hat{d}_j^\dagger \hat{d}_j + \frac{1}{4} \sum_{j=1} (\hat{d}_j^\dagger \hat{d}_{j+1} + \hat{d}_j^\dagger \hat{d}_{1+j}^\dagger) + \text{H.c.},$$

$$\hat{H}_B = -\frac{1}{2} \sum_{j=1} \hat{d}_j^\dagger \hat{d}_j - \frac{1}{4} \sum_{j=1} (\hat{d}_j^\dagger \hat{d}_{j+1} + \hat{d}_j^\dagger \hat{d}_{1+j}^\dagger) + \text{H.c.}$$

with two independent sets of fermionic creation(annihilation) operators $\hat{d}^\dagger(\hat{d})$ and $\hat{d}^\dagger(\hat{d})$. The subsystems describes two independent systems, each corresponding to one instance of Kitaev's model for a p -wave paired superconductor [4] at the boundary point between the trivial and topological phase (see the Supplemental Materials [57] Sec. I). Exactly at the Kitaev points, only one of the subsystems A or B contributes energy in the Hamiltonian so the full system acquires one free spin per unit cell, leading to groundstate degeneracies $2^{L/2}$ and $2^{L/2-1}$ for open and closed chains, respectively [6]. For the open chain this amounts to $L/2$ Majorana operators, which are entirely absent from the Hamiltonian, so that the entire spectrum exhibits the same degeneracies as found in the ground state. This global degeneracy is a stronger condition than what is usually required for general topological order [58]. The system here hosts multiple bulk Majorana modes distributed all across the chain, with a hierarchy of multiply degenerate states. Specifically, the highly degenerate ground-state multiplet is separated from the excited states by a gap, a necessary condition for the presence of non-Abelian quasiparticles [2,3]. Throughout the text, a *globally* N -fold degenerate spectrum means that each level in the spectrum is *at least* N -fold degenerate, but additional degeneracies may be present.

In this work, we focus specifically on the realization of MEMs around the Kitaev point $\theta_{\text{KP}} = \pi/2$. In Kitaev's original model, the MEM phase supports topologically protected modes at the edges [4], which correspond to a spontaneously broken spin-reflection symmetry when mapped to the Ising spin model [7]. We will nevertheless use the term MEM also in the spin picture.

A. Majorana edge modes via perturbative interactions

To achieve the MEM phase in our setup we must invoke an additional term \hat{V}_δ into the Hamiltonian. To find the appropriate perturbations we start at the Kitaev point $\theta_K = \pi/2 \rightarrow K = 1$, where only subsystem A enters the full Hamiltonian. To help the discussion, we temporarily invoke a more general form of the fermionic Hamiltonian of subsystem A:

$$\hat{H}_A = \frac{K_1}{2} \sum_{j=1} \hat{d}_j^\dagger \hat{d}_j + \frac{K_2}{4} \sum_{j=1} (\hat{d}_j^\dagger \hat{d}_{j+1} + \hat{d}_j^\dagger \hat{d}_{1+j}^\dagger) + \text{H.c.} \quad (3)$$

For our case we currently have $K_1 = K_2 = 1$, and j is the unit cell index (see the Supplemental Materials [57] Sec. I). As noted before, this gives the boundary point between the trivial and the topological phase of the Kitaev model [4]. Therefore, for topological modes the relative size of the first term must be decreased, so that $|K_1| < K_2$. We may thus either decrease $|K_1|$ or increase K_2 to enter the topological regime.

We first consider the (local) energy term proportional to K_1 and map this back to the spin picture (see the Supplemental Materials [57] Sec. II), revealing the appropriate perturbation

term,

$$\hat{V}_\delta^{\text{intra}} = \delta \sum_{j=1}^{L/2} \hat{S}_{2j-1}^x \hat{S}_{2j}^x, \quad (4)$$

with the MEM phase occurring for $|K_1 + \delta| < K_2$. This term corresponds to interactions *within* a unit cell of two spins. We can compare this situation to the equivalence of the transverse-field Ising model and the Kitaev model [7,59], where the local fermionic energy term maps onto the local energy of a single spin in a magnetic field. For our case, each term in Eq. (4) instead represents the local energy of the unit cell dimer j . Precisely at the Kitaev point, where $K_1 = K_2 = 1$, the dimer energy equals that of the interdimer bond, and the system remains gapped for $L \rightarrow \infty$. Here the global degeneracy is that of $L/2$ dimers with one free spin each, giving $2^{L/2}$ states. For $|K_1| < K_2$ the interdimer bonds instead dominate, and an additional global twofold symmetry arises for $L \rightarrow \infty$, corresponding to zero-energy Majorana modes, giving a global degeneracy of $2 \times 2^{L/2}$. The degeneracy is perfect in the limit of infinite chains, whereas the finite-size gap between the two degenerate multiplets scales with $e^{-L/2}$. Aside from additional degeneracies, the energy spectrum of this system coincides perfectly with that of a transverse field Ising model with $L/2$ spins, $\hat{H}_I = \sum K_2 \hat{S}_i^y \hat{S}_{i+1}^y + K_1 \hat{S}_i^x$. The Hamiltonian (1) is thus very similar to the transverse field Ising model but differs in its dynamical properties due to the additional degeneracies.

As noted above, we can also enter the MEM phase by increasing the relative size of the terms scaling with K_2 in the Hamiltonian (3), giving

$$\hat{V}_\delta^{\text{inter}} = \delta \sum_{j=1}^{L/2} \hat{S}_{2j}^y \hat{S}_{2j+1}^y, \quad (5)$$

with the unit cell index j and the MEM phase occurring for $|K_1| < K_2 + \delta$. This term corresponds to interactions *between* two unit cells.

We now invoke a third option for the perturbing interaction, \hat{V}_δ , corresponding to a *fully connected* Ising term,

$$\hat{V}_\delta^{\text{Ising}} = \delta \sum_{i=1}^L \hat{S}_i^y \hat{S}_{i+1}^y, \quad (6)$$

where i is the spin site index. This perturbation does not map the fermionic Hamiltonian onto a Kitaev model, but we nevertheless see the emergence of an MEM phase for $|K_1| < K_2 + \delta$. We will see that this perturbation simultaneously creates MEMs and breaks local symmetries within each dimer, giving rise to a beating pattern in the time-dependent edge spin correlation functions. In conclusion, we use δ as an effective parameter that controls the onset of MEMs, using either of the perturbations in Eq. (5) or Eq. (6). The two different perturbations are used to highlight two different effects in dynamical simulations of the MEM regime. The spectrum due to the interdimer perturbation (5) is depicted in Fig. 1. We want to treat all choices of perturbation on equal footing and study the systems dynamics in the spin picture. Therefore, although the fermion mapping could be employed to solve the system for the perturbations in Eqs. (4) and (5), we will in the following exclusively employ the spin picture.

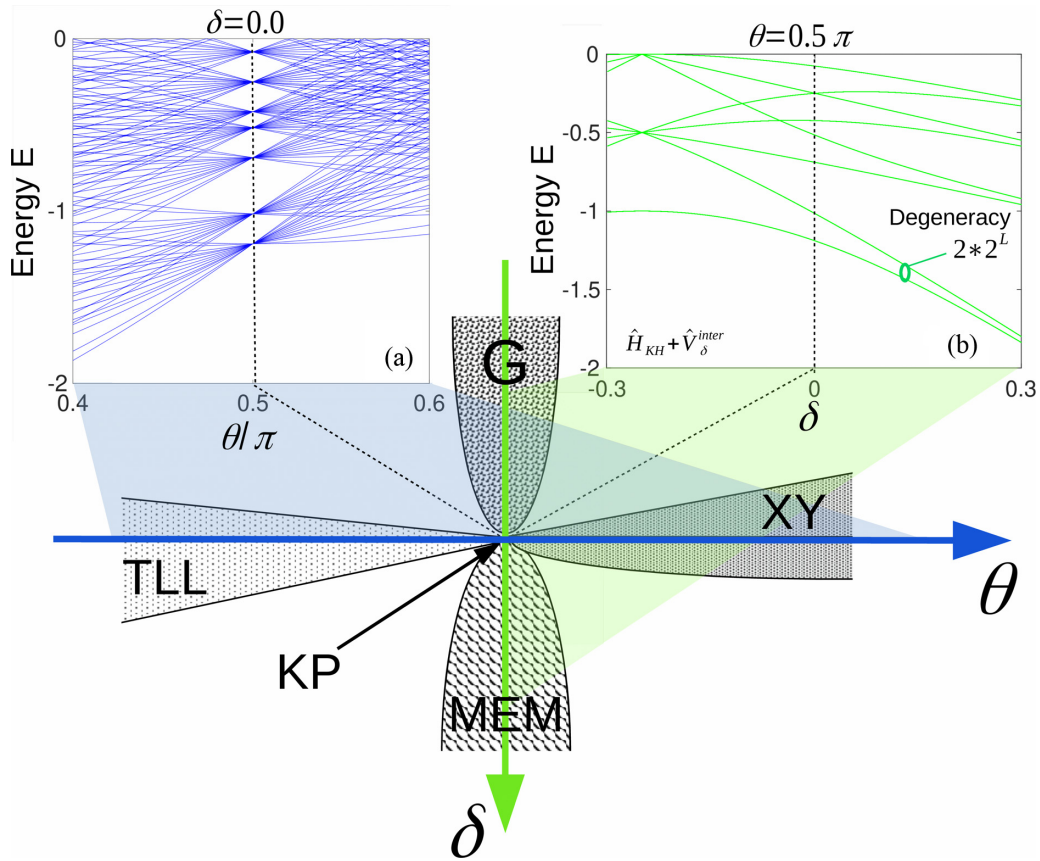


FIG. 1. Phase diagram of the anisotropic Kitaev-Heisenberg (KH) quantum spin model for $L = 8$ in the vicinity of a critical Kitaev point (KP), located at $(\delta = 0, \theta = \pi/2)$. Here the Hamiltonian supports a degenerate ground state with multiple Majorana modes. The hierarchy of degenerate multiplets at the KP is directly observed in the spectrum in panel (a). Adding a term \hat{V}_δ with strength $\delta > 0$ drives the system into the Majorana edge mode (MEM) phase, giving rise to a bulk gap, dividing all energy states into two sectors. Perturbing around the KP with the Y-bond interaction term $\hat{V}_\delta^{\text{inter}}$ in Eq. (5) realizes a dimer Majorana edge mode phase, with each level attaining a 2×2^L degeneracy for $L \rightarrow \infty$, whereas a nonvanishing gap is attained for finite L , as seen in panel (b). For $\theta = \pi/2 - d\theta$ and $\delta \sim 0$, shown in (a), the system becomes a Tomonaga Luttinger liquid (TLL), which persists for moderate perturbation strengths $|\delta|$. For $\theta = \pi/2 + d\theta$ and $\delta \sim 0$, the system is in a spiral XY phase, also persisting for moderate perturbations. For $\theta \sim \pi/2$ and $\delta < 0$, the system is in a gapped (G) phase with no MEMs. The MEM phases show a distinctly different behavior than the other phases in terms of the dynamical development of local spins.

III. PHASE DIAGRAM AND STATIC PROPERTIES

Let us now briefly discuss the four phases in the phase diagram shown in Fig. 1, spanned by the parameters θ and δ in the vicinity of the critical Kitaev point at $\theta = \pi/2$ and $\delta = 0$. The characterization of these phases will be helpful when discussing the dynamical features of local spins in the later sections:

(1) Majorana edge mode (MEM) phase ($\theta = \theta_{\text{KP}} = \pi/2, \delta > 0$): the bulk energy spectrum in this regime is gapped, with two zero-energy edge modes in the thermodynamic limit. However, in finite systems, their energies remain small but finite, yielding a finite-size gap that vanishes exponentially with increasing system size. For the perturbing term, $\hat{V}_\delta^{\text{inter}}$, each level has a global $2^{L/2}$ -fold degeneracy due to free parameters in the Hamiltonian, so that for $L \rightarrow \infty$ the spectrum becomes $2 \times 2^{L/2}$ -fold degenerate. We call this the *dimer* MEM phase. For $\hat{V}_\delta^{\text{Ising}}$ the spectrum becomes globally twofold degenerate for $L \rightarrow \infty$. We call this the *Ising* MEM phase. In the MEM phase, the corresponding free fermion model supports topological edge modes.

(2) Gapped (G) phase ($\theta = \theta_{\text{KP}} = \pi/2, \delta \lesssim 0$): this regime has a gapped energy spectrum, with no Majorana edge modes present.

(3) Spiral XY phase ($\theta > \theta_{\text{KP}} = \pi/2, \delta = 0$): the energy spectrum in this regime is gapless, and no Majorana modes are present.

(4) Tomonaga Luttinger liquid (TLL) phase ($\theta < \theta_{\text{KP}} = \pi/2, \delta \approx 0$): The low-energy spectrum is gapless.

Further characterization and discussion of the static properties of these phases are presented in the Supplemental Materials [57] Sec. III.

IV. DYNAMICAL FOOTPRINTS OF THE MAJORANA MODES

Time-dependent observables are a powerful tool for the analysis of physical systems beyond their ground-state phases [42,44,45,48,50]. In particular, local measurements, $\hat{S}_i^D(t)$, of a spin i along $D \in \{x, y, z\}$ are intuitive and experimentally accessible probes that can be used to highlight the emergence of MEMs [50,60].

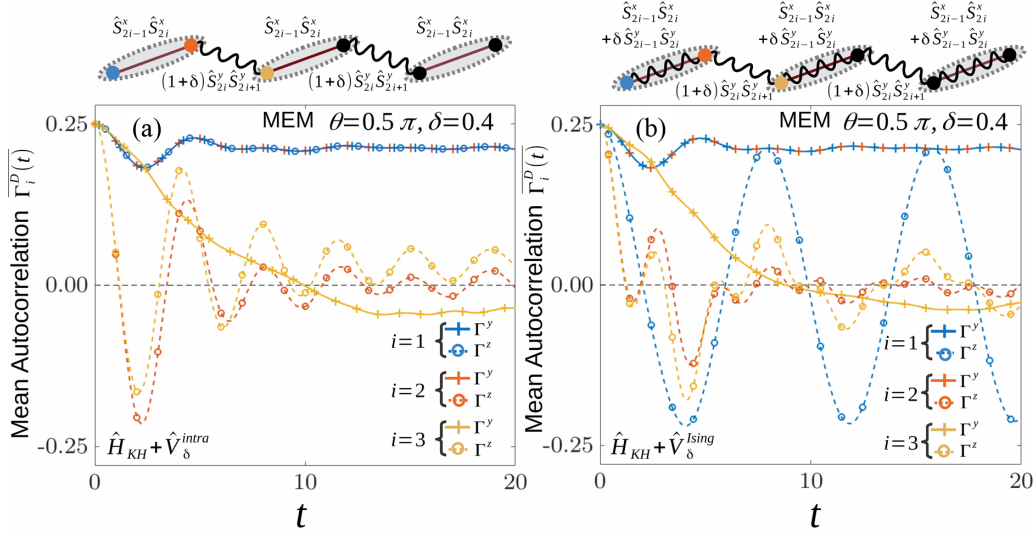


FIG. 2. Time evolution of mean autocorrelation $\overline{\Gamma_i^D(t)}$ at an edge site, $i = 1$, and at a bulk sites, $i = 2$, $i = 3$ for a system of $L = 14$ spins. (a) The mean autocorrelation function in the MEM phase achieved for $\hat{H}_\delta^{\text{inter}} = \hat{H}_{\text{KH}}(\theta = \pi/2) + \hat{V}_\delta^{\text{inter}}$ with $\delta = 0.4$. Both $i = 1$ and $i = 2$ show long-time coherence for a spin initially pointing in the y direction, owing to the presence of zero modes which commutes with \hat{H} up to an exponentially small factor ϵ . This is also true for spin z , but only at the edge. Other spins decay. (b) The corresponding autocorrelations for $\hat{H}_\delta^{\text{sing}} = \hat{H}_{\text{KH}}(\theta = \pi/2) + \hat{V}_\delta^{\text{sing}}$. Here the autocorrelation $\overline{\Gamma_i^z(t)}$ for an edge spin $i = 1$ along z oscillates perpetually with an amplitude scaling with the corresponding value of $\overline{\Gamma_i^y(t)}$. We emphasize that, in both plots, the decaying spins would go to zero for $L \rightarrow \infty$ and $t \rightarrow \infty$.

We first consider the spin operator,

$$\hat{G}^D = \prod_{k=1}^L \hat{\sigma}_k^D. \quad (7)$$

The eigenstates of \hat{G}^D are denoted $|\pm \Phi_n^D\rangle = [|s_1^D s_2^D s_3^D \dots\rangle]$. These state are parity eigenstates, where we use \pm to denote positive or negative parity, respectively. These eigenstates will serve as the initial states for the dynamical simulations, where we numerically evolve each state in time under the Hamiltonian operator (1) and study the dynamical evolution of local spins. We also note that this spin-operator flips all spins along the axes perpendicular to D , i.e., along x and y for \hat{G}_z .

For quantitative measures, we consider the mean autocorrelation function,

$$\overline{\Gamma_i^D(t)} = (1/N) \sum_{n=1}^N \Gamma_{i,n}^D(t) = (1/N) \sum_{n=1}^N \langle \hat{S}_i^D(t) \hat{S}_i^D(t=0) \rangle_n, \quad (8)$$

where the sum over N produces the average over a randomly sampled set of N initial states $|\pm \Phi_n^D\rangle \in \{|\downarrow\downarrow\downarrow\downarrow \dots\rangle, \dots, |\downarrow\uparrow\downarrow\uparrow \dots\rangle\}$ in the basis of spin D . We also consider the (discrete) Fourier transformed evolution functions $\mathcal{F}(\langle \hat{S}_i^D(t) \rangle_n)$, again taking the average over a large set of initial states,

$$|c_i^D(\omega)| = (1/N) \left| \sum_{n=1}^N \mathcal{F}(\langle \hat{S}_i^D(t) \rangle_n) \right|. \quad (9)$$

We further calculate variances to highlight which features are largely independent of the particular input states we

choose.¹ By sampling over multiple initial states and taking the average, we specifically access robust features of the system in the sense that an experimental setup would not rely on repeated and deterministic preparation of any specific initial state. Measurements can instead be performed with mixed states for those spins which are not directly probed, which is especially relevant for detection of *strong zero modes* [29,50]. To simplify the computations we, however, consider pure initial states for the individual runs and take the average afterward, i.e., we essentially perform a Monte Carlo sampling of a completely mixed density matrix. Figure 2 shows mean autocorrelations for a set of randomly sampled states developing in time under two different Hamiltonians. As will be discussed in the following section, there are several robust features in the mean autocorrelations of edge spins (like the constant spin- y projection in each plot), even though they essentially represent time development of mixed states.

A. Zero modes of the Hamiltonian

A Hamiltonian that supports MEMs can be represented in terms of Majorana operators in such a way that some of them drop out of the Hamiltonian in the infinite ($L \rightarrow \infty$) system limit [4], giving rise to global symmetries and corresponding degeneracies in the entire energy spectrum. In line with the procedures in Refs. [4,49,50], we elucidate the dynamical properties of the finite-size system by first deriving the zero

¹Because of computational limitations, the frequency-dependent quantities are generally displayed on rather coarse grids in frequency. We stress, however, that the significant features, which will be used to identify the MEM phases, are visible already for rather short evolution times. To extract more detailed information we run simulations for longer times.

modes, which correspond to the Majorana modes in the corresponding fermionic model. These modes are constructed to approximately commute with the Hamiltonian, with corrections $\sim e^{-L}$, and are associated with long-time coherent features in the dynamical evolution.

We first consider the Hamiltonian (1) at the Kitaev point $\theta = \pi/2$, using the perturbation $\hat{V}_\delta^{\text{inter}}$, so that

$$\begin{aligned}\hat{H}_\delta^{\text{inter}} &= \hat{H}_{\text{KH}}(\theta = \pi/2) + \hat{V}_\delta^{\text{inter}} \\ &= \sum_{j=1}^{L/2} (\hat{S}_{2j-1}^x \hat{S}_{2j}^x + \hat{S}_{2j}^y \hat{S}_{2j+1}^y) + \delta \sum_{j=1}^{L/2} \hat{S}_{2j}^y \hat{S}_{2j+1}^y \\ &\equiv (1 + \delta)(\hat{H}_0 + \hat{W}).\end{aligned}\quad (10)$$

For convenience, we have rescaled the Hamiltonian in the last line, so we end up with

$$\hat{H}_\delta^{\text{inter}} \rightarrow \hat{H}_0 + \hat{W}, \quad \hat{H}_0 = \sum_{j=1}^{L/2} \hat{S}_{2j}^y \hat{S}_{2j+1}^y, \quad \hat{W} = \frac{1}{1 + \delta} \sum_{j=1}^{L/2} \hat{S}_{2j-1}^x \hat{S}_{2j}^x,$$

where we recognize that $\delta > 0$ yields the dimer MEM phase.

We now proceed to analytically constructing the zero modes for a set of different operators. We start by considering a spin observable that commutes with the Hamiltonian \hat{H}_0 and from there we proceed to construct higher-order terms as to build a mode that commutes, up to a small correction, with the full Hamiltonian. As a first example, we take a local spin along y at the edge of the spin chain as the zeroth-order approximation of the mode operator $\Psi_A^{(0)} = \hat{S}_1^y$, which clearly commutes with the dominant term \hat{H}_0 in the Hamiltonian (10). It does, however, not commute with the full Hamiltonian, and for $\hat{H}_0 + \hat{W}$ we find

$$[\hat{H}_\delta^{\text{inter}}, \Psi_A^{(0)}] = i \frac{1}{1 + \delta} \hat{S}_1^z \hat{S}_2^x.$$

We can offset this by introducing first- and second-order terms to the mode operator $\Psi_A^{(1)} = \mathcal{M}_1 \hat{S}_1^z \hat{S}_2^y$ and $\Psi_A^{(2)} = -4[1/(1 + \delta)] \hat{S}_1^z \hat{S}_2^y \hat{S}_3^y$ so that

$$[\hat{H}_0, \Psi_A^{(1)} + \Psi_A^{(2)}] = -4 \frac{1}{1 + \delta} [\hat{S}_2^y \hat{S}_3^y, \Psi_A^{(2)}] = -i \frac{1}{1 + \delta} \hat{S}_1^z \hat{S}_2^x,$$

where the factor of four is absorbed by an emerging operator $\hat{S}_3^y \hat{S}_3^y = 1/4$. The first-order term always commutes with the full Hamiltonian, so we can freely choose the constant \mathcal{M}_1 . $\Psi_A^{(2)}$ does not commute with \hat{W} , but results in a higher-order term when commuting the mode the Hamiltonian. This can again be offset by adding additional terms of higher order into the mode. Continuing in this fashion until we reach the end of the chain we finally get (see the Supplemental Materials [57] Sec. IV)

$$\begin{aligned}\Psi_A &= \sum_{j=1}^{L/2} \Psi_A^{(2j)} + \sum_{j=2}^{L/2} \Psi_A^{(2j-1)} = \mathcal{N}_e \sigma_1^y + \mathcal{N}_e \sum_{j=2}^{L/2} \left(-\frac{1}{1 + \delta} \right)^{j-1} \\ &\quad \times \sigma_{2j-1}^y \prod_{k=1}^{2j-2} \sigma_k^z + \mathcal{N}_o \sum_{j=1}^{L/2} \mathcal{M}^{j-1} \sigma_{2j}^y \prod_{k=1}^{2j-1} \sigma_k^z,\end{aligned}\quad (11)$$

which we can show commutes with the Hamiltonian up to an exponentially small factor. The constants \mathcal{N}_0 and \mathcal{N}_e are

normalization constants, found by setting $\Psi_A^2 = 1$. In this expression, we have changed the representation to Pauli spin operators, $\hat{S}_i^D \rightarrow \sigma_i^D/2$, and separated the odd and even orders for convenience. Each term in the sums now corresponds to a Majorana fermion [4]. For the second sum we have one free choice for the constant \mathcal{M}_i per term, meaning each unit cell adds a degree of freedom for the zero mode. This is consistent with the global $2^{L/2}$ -fold degeneracy in the spectrum. For simplicity, we have chosen $\mathcal{M}_j = \mathcal{M}^{j-1}$.

Each term in the sum of Eq. (11) anticommutes with all the others, so that

$$\begin{aligned}\Psi_A^2 &= \mathcal{N}_e^2 \frac{1 - \left(\frac{1}{1+\delta}\right)^L}{1 - \left(\frac{1}{1+\delta}\right)^2} + \mathcal{N}_o^2 \frac{1 - \mathcal{M}^L}{1 - \mathcal{M}^2} \\ &\approx \mathcal{N}_e^2 \frac{1}{1 - \left(\frac{1}{1+\delta}\right)^2} + \mathcal{N}_o^2 \frac{1}{1 - \mathcal{M}^2},\end{aligned}\quad (12)$$

and we proceed to choose the normalization so that $\Psi_A^2 = 1$ for $|\mathcal{M}| < 1$ and $\delta > 0$. It is now clear the each of the zero modes constructed in Eq. (11) commutes with the Hamiltonian H , now in matrix representation, up to an exponentially small term,

$$\begin{aligned}[\hat{H}_\delta^{\text{inter}}, \Psi_A] &= \left[\frac{\sigma_{L-1}^x \sigma_L^x}{1 + \delta}, \mathcal{N}_e \left(-\frac{1}{1 + \delta} \right)^{\frac{L}{2}-1} \sigma_{L-1}^y \prod_{k=1}^{L-2} \sigma_k^z \right] \\ &= 2i \frac{\mathcal{N}_e}{1 + \delta} \left(-\frac{1}{1 + \delta} \right)^{\frac{L}{2}-1} \left(\prod_{k=1}^{L-1} \sigma_k^z \right) \sigma_L^x \\ &= -2 \frac{\mathcal{N}_e}{1 + \delta} \left(-\frac{1}{1 + \delta} \right)^{\frac{L}{2}-1} \mathcal{G}^z \sigma_L^y = \varepsilon_{\text{rem}},\end{aligned}\quad (13)$$

where \mathcal{G}^z is the spin-flip operator in Eq. (7). We also note that the zero mode anticommutes with the spin-flip operator so that $\{\mathcal{G}^z, \Psi_A\} = 0$. This means that \mathcal{G}^z toggles between different eigenstates of Ψ_A and vice versa. Together with normalizability and the vanishing commutator ε_{rem} , these properties of the zero mode constitute the necessary conditions for long-time edge spin coherence [50]. Alternatively, zero modes can be constructed similarly by starting at the other edge, \hat{S}_L^y .

We also find that for \hat{S}_2^y and \hat{S}_1^z , which also commute with \hat{H}_0 , two corresponding zero modes, Ψ_B and Ψ_C can be found (see the Supplemental Materials [57] Sec. IV). These modes differ in their construction, since they are each derived from different starting points. However, the different zero modes Ψ_A , Ψ_B , and Ψ_C each span the same operator space, so that the implicated global degeneracy of the energy spectrum for $L \rightarrow \infty$ is still $2 \times 2^{L/2}$. In summary, we can construct normalizable zero modes Ψ_A , Ψ_B , and Ψ_C for the Hamiltonian (10), which includes the perturbation $\hat{V}_\delta^{\text{inter}}$ with $\delta > 0$.

Interestingly, the zero modes Ψ_A and Ψ_B also commute, up to an exponentially small factor, with the alternative Hamiltonian

$$\hat{H}_\delta^{\text{Ising}} = \hat{H}_{\text{KH}}(\theta = \pi/2) + \hat{V}_\delta^{\text{Ising}},\quad (14)$$

which instead uses the perturbing Ising term $\hat{V}_\delta^{\text{Ising}}$. This is true for $\delta > 0$, providing we set all constants in front of odd orders to zero, so that $\mathcal{M}_A = 0$ and $\mathcal{M}_B = 0$. This means that for each of the operators, \hat{S}_1^y, \hat{S}_2^y , one may use the same construction of zero modes for Hamiltonian $\hat{H}_\delta^{\text{Ising}}$ as for

$\hat{H}_\delta^{\text{inter}}$. However, for this choice of perturbation $\hat{H}_\delta^{\text{Ising}}$ the free parameters \mathcal{M}_i for the previously constructed zero modes are removed, so the global degeneracy in the spectrum becomes only twofold in the limit $L \rightarrow \infty$, resulting in different behavior in the dynamical simulations.

The commutations between the finite-size zero modes and the Hamiltonians $\hat{H}_\delta^{\text{Ising}}$ and $\hat{H}_\delta^{\text{inter}}$ are identical, so the finite-size gap between zero modes, i.e., the energy gap associated with the nonzero commutation between the zero mode and the Hamiltonian $\Delta_L = E_1 - E_0$, are also the same for the different perturbations. We will see that the long-time coherence depends crucially on this gap, and we therefore expect some identical long-time features for both Hamiltonians.

B. Long-time dynamics of edge spins

We now proceed to summarize the impact of zero modes on the long-time dynamics of our system. For details, we refer the reader to the Supplemental Materials [57] Sec. V, and for a comprehensive theoretical background to Refs. [49,50]. We evaluate the autocorrelation function $\Gamma_1^D(t)$ for an eigenstate $|S^D\rangle$, with corresponding eigenvalue s_1^D , of the edge spin operator \hat{S}_1^D along direction D . In practice we will use states $|\pm \Phi_n^D\rangle$ which are eigenstates of \mathcal{G}^D , but here we consider a general state $|S^D\rangle$. We get for the autocorrelation

$$\begin{aligned} \Gamma_1^D(t) &= \langle S^D | \hat{S}_1^D(t) \hat{S}_1^D(t=0) | S^D \rangle \\ &= \frac{s_1^D}{2} \sum_{n,m} e^{-it(E_m - E_n)} \langle S^D | n \rangle \langle n | \sigma_1^D | m \rangle \langle m | S^D \rangle, \end{aligned} \quad (15)$$

where $|n\rangle, |m\rangle$ are eigenstates of some Hamiltonian \hat{H} with corresponding zero mode Ψ_A . Since Ψ_A (almost) commutes with the Hamiltonian we may divide all energy states into two sectors denoted by positive or negative sign, corresponding positive or negative eigenvalues of Ψ_A so that

$$\hat{H}|n_\pm\rangle \approx E_n|n_\pm\rangle, \Psi_A|n_\pm\rangle = \pm|n_\pm\rangle, \quad (16)$$

We can now rewrite the autocorrelation function with new indices

$$\begin{aligned} \Gamma_1^D(t) &= s_1^D \sum_{n,m} e^{-i(E_m - E_n)t} (\langle S^D | (|n_+\rangle\langle n_+| + |n_-\rangle\langle n_-|) \\ &\quad \times \sigma_1^D (|m_+\rangle\langle m_+| + |m_-\rangle\langle m_-|) | S^D \rangle). \end{aligned}$$

For long times t and large system size L , terms with $E_n \neq E_m$ add up incoherently while terms with $E_n = E_m$ add up coherently, i.e., terms with $E_n \neq E_m$ get a random phase so that we can ignore them. The double sum may then be approximated for long times by

$$\Gamma_1^D(t) \approx s_1^D \sum_n (T_1^D + T_2^D + T_3^D + T_4^D) \quad (17)$$

with terms $T_1^D - T_4^D$ relating to the time-independent matrix elements between $|n_\pm\rangle$:

$$\begin{aligned} T_1^D &= \langle S^D | n_- \rangle \langle n_- | \sigma_1^D | n_- \rangle \langle n_- | S^D \rangle, \\ T_2^D &= \langle S^D | n_- \rangle \langle n_- | \sigma_1^D | n_+ \rangle \langle n_+ | S^D \rangle, \\ T_3^D &= \langle S^D | n_+ \rangle \langle n_+ | \sigma_1^D | n_- \rangle \langle n_- | S^D \rangle, \\ T_4^D &= \langle S^D | n_+ \rangle \langle n_+ | \sigma_1^D | n_+ \rangle \langle n_+ | S^D \rangle. \end{aligned} \quad (18)$$

This shows that for an infinite system, the long-time spin oscillations are stable. For finite systems this is no longer the case, and the oscillations will eventually decay. The coherence time, i.e., the time during which the spin autocorrelation function remains stable, either displaying a finite value or a persistent oscillation, is generally set by the commutation between the Hamiltonian and the zero mode, which vanishes with $L \rightarrow \infty$ [50]. Interestingly, if the finite-size gaps Δ_L between semidegenerate states in a system's spectrum are all identical, spin autocorrelations which first appear to decay will have a revival time of order $1/\Delta_L \propto 1/\langle \varepsilon_{\text{rem}} \rangle$. If all gaps are different we will instead have only partial revivals. For integrable systems, like the Ising model, these revival times may be directly calculated [61]. This is also true for the Hamiltonian in Eq. (10), which will be apparent from the dynamical simulations. We stress that we employ a closed quantum system where revivals do occur after an initial decay. However, these happen at exponentially long times that are controlled by the system size. Before such revivals, equilibration processes occur that are due to the scattering between modes [62].

So far we have not specified the direction D in which we aim to measure the spin, and we proceed to study the effect of two particular choices of \hat{S}_1^D . We here aim to explain the behavior of different spin observables by invoking the expression for the autocorrelation (17) and explicitly evaluating the matrix elements in Eq. (18). Since we specifically use the Pauli-spin representation of operators in this chapter, we will use σ_i^D to represent a spin operator at site i along D . We begin with the Hamiltonian $\hat{H}_\delta^{\text{inter}}$ and σ_1^y (spin measured in the y direction) with the corresponding zero mode Ψ_A derived in the pervious section. To evaluate the matrix elements T_2^y and T_3^y we exploit the spin-flip operator in Eq. (7) which anticommutes with Ψ_A so that $\mathcal{G}^z|n_\pm\rangle = |n_\mp\rangle$ and we get

$$\begin{aligned} T_2^y &= \langle S^y | n_- \rangle \langle n_+ | S^y \rangle \times \langle n_+ | \{ \sigma_1^y, \mathcal{G}^z \} | n_+ \rangle / 2, \\ T_3^y &= \langle S^y | n_+ \rangle \langle n_- | S^y \rangle \times \langle n_+ | \{ \sigma_1^y, \mathcal{G}^z \} | n_+ \rangle / 2. \end{aligned} \quad (19)$$

Now we note the anticommutation $\{ \sigma_1^y, \mathcal{G}^z \} = 0$, leading to $T_2^y = T_3^y = 0$. For T_1^y and T_4^y we instead employ Eq. (16):

$$\begin{aligned} T_1^y &= |\langle S^y | n_- \rangle|^2 \times \langle n_+ | \{ \Psi_A, \mathcal{G}^z \sigma_1^y \mathcal{G}^z \} | n_+ \rangle / 2, \\ T_4^y &= |\langle S^y | n_+ \rangle|^2 \times \langle n_+ | \{ \Psi_A, \sigma_1^y \} | n_+ \rangle / 2. \end{aligned} \quad (20)$$

For T_4^y we may use Eq. (11) directly, giving $\{ \Psi_A, \sigma_1^y \} = \mathcal{N}_e + \mathcal{C}$, where \mathcal{C} represents (exponentially) small corrections. For T_1^y we see that $\{ \Psi_A, \mathcal{G}^z \sigma_1^y \mathcal{G}^z \} = \{ \Psi_A, \sigma_1^z \sigma_1^y \sigma_1^z \} = -\{ \Psi_A, \sigma_1^y \}$. This gives the long-time limit of the autocorrelation

$$\Gamma_1^y(t) \approx s_1^y (\mathcal{N}_e + \mathcal{C}) \sum_n (|\langle S^y | n_+ \rangle|^2 - |\langle S^y | n_- \rangle|^2), \quad (21)$$

which depends on only the initial state and how much overlap it has with each sector of eigenstates for Ψ_A . The exact form of the corrections \mathcal{C} depend specifically on the model [50], but they are always exponentially decreasing with $L/2$.

We can use an identical derivation for σ_2^y by making the substitutions $\Psi_A \rightarrow \Psi_B$ and redefining the quantum number n so that $\Psi_B|n_\pm\rangle = \pm|n_\pm\rangle$. For σ_1^z we instead put $\mathcal{G}^z \rightarrow \mathcal{G}^x$, $\Psi_A \rightarrow \Psi_C$ and $\Psi_C|n_\pm\rangle = \pm|n_\pm\rangle$.

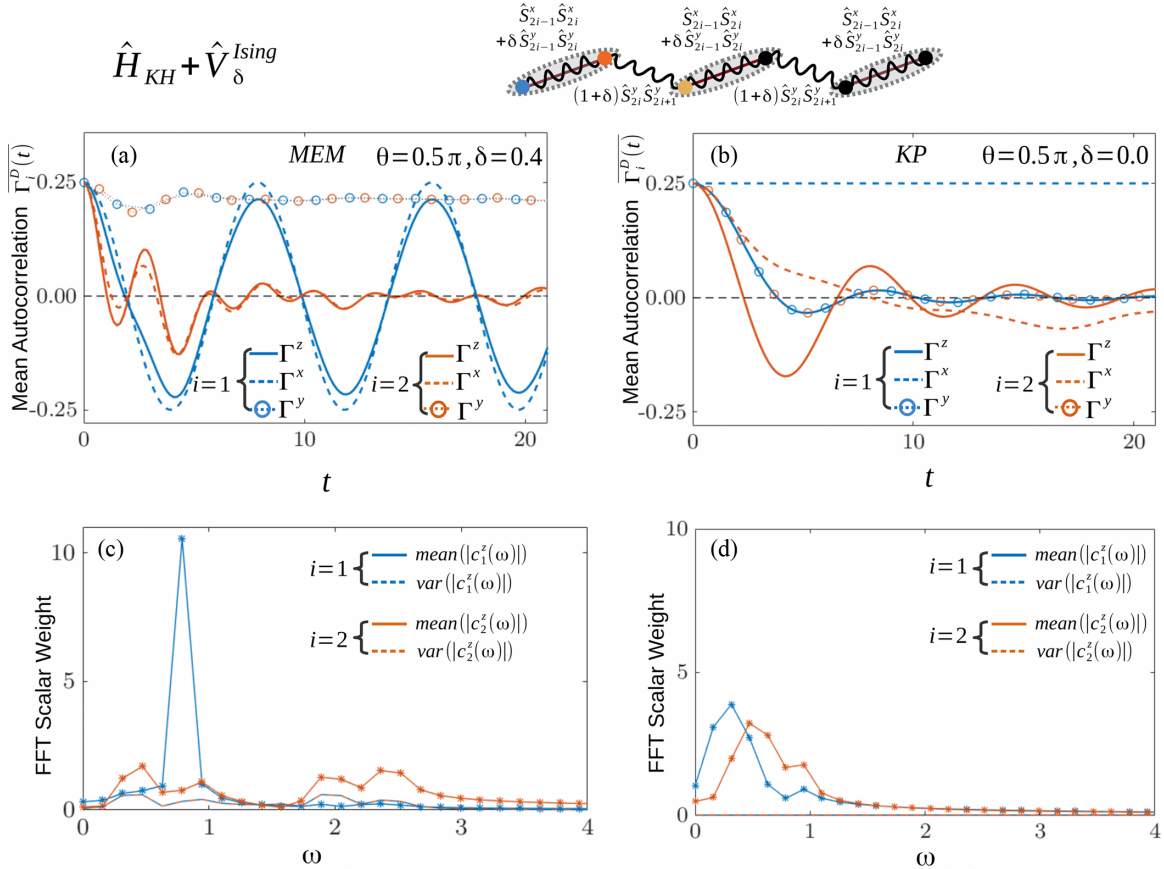


FIG. 3. Time evolution of mean autocorrelation $\overline{\Gamma_i^D(t)}$ at an edge site, $i = 1$, and at a bulk site, $i = 2$ for a system of $L = 14$ spins. (a), (b) The mean autocorrelation function (8) in the Ising MEM phase and at the Kitaev point, respectively. The former has Majorana modes only at the edges, and the latter has one Majorana mode per unit cell throughout the bulk. In the MEM phase, a single dominant oscillation frequency is observed for the edge site. This spin precession is only weakly damped, whereas oscillations in the bulk decay fast. At the critical point (b), no characteristic frequency is observed. (c), (d) The frequency Fourier components ω (9) of the local spin-expectation value, $\langle \hat{S}_i^z(t) \rangle$, averaged over the same set of initial states as for the autocorrelation functions, for the MEM phase (c) and the Kitaev point (d). Also shown are the corresponding variances. The dominant single peak for the edge site $i = 1$ has low relative variance and indicates a single oscillation frequency, which is independent of system size, L . The bulk site $i = 2$ has a strikingly different behavior, with several oscillation frequencies and higher relative variances. The details of the frequency profile are dependent on system size, indicative of a bulk mode. (d) The characteristic behavior of the Kitaev point, with a multi-peaked structure and zero variance at both edge and bulk sites.

Figure 2(a) shows the simulated dynamical development of spins for $\hat{H}_\delta^{\text{inter}}$, confirming that the mean autocorrelation for σ_1^y , σ_2^y , and σ_1^z is long-lived compared to other spins. This is directly explained by the fact that we can construct corresponding zero modes, as shown in the previous section. This is not true for the other operators shown in the plot, where the autocorrelation vanishes for long times.

C. Beating patterns for edge spins

In Fig. 2 we study how the autocorrelation function compares for the Hamiltonians $\hat{H}_\delta^{\text{inter}}$ and $\hat{H}_\delta^{\text{Ising}}$. The results for σ_1^y and σ_2^y are the same for the different Hamiltonians, whereas σ_1^z is strikingly different. Curiously, long-time coherence is still present for $\hat{H}_\delta^{\text{Ising}}$, but with an oscillating factor which we find is independent of system size. The coherence time of the oscillation is however set by system size, as for σ_1^y and σ_2^y .

We can relate this result directly to the zero modes. We derive in the Supplemental Materials [57] Sec. VI

that

$$\Gamma_1^z(t) \approx \frac{s_1^z}{4} (\cos^2 \delta t - \sin^2 \delta t) (\mathcal{N}_e + C) \times \sum_n (|\langle S^z | n_+ \rangle|^2 - |\langle S^z | n_- \rangle|^2). \quad (22)$$

We see that the expression by symmetry is, except for the time-dependent factor, identical to the autocorrelation $\Gamma_1^y(t)$, but here for an initial state $|S^z\rangle$. This precession of the edge spin σ_1^z is hence given by an oscillation, with frequency δ , and an envelope function given by the coherence time of σ_1^y .

Comparing the evolution of different spin-components in Fig. 3(a) we see that σ_1^x has a spin precession which does not decohere, in contrast to σ_1^z . We note that the x component of the edge spin commutes with $\hat{H}_{\text{KH}}(\theta = \pi/2)$, and using the same technique as for σ_1^z one may again calculate the spin precession of σ_1^x from the perturbation $\hat{V}_\delta^{\text{Ising}}$. This gives a time dependence $\propto (\cos^2 \delta t - \sin^2 \delta t)$ without any decoherence,

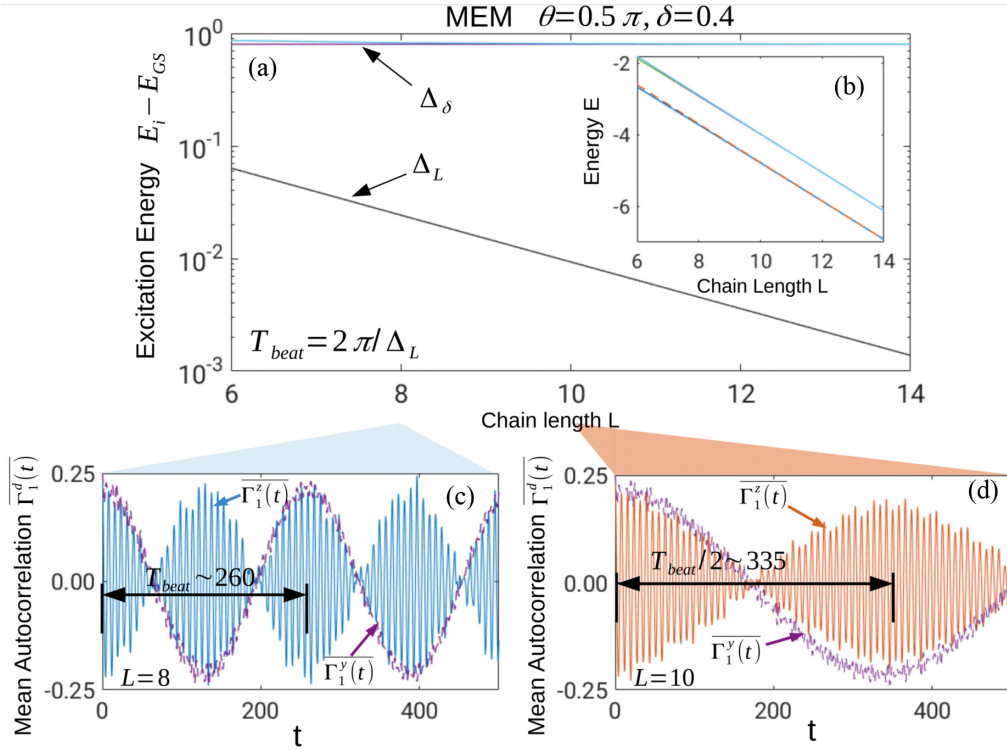


FIG. 4. Comparison of static energy gaps and the mean autocorrelation $\overline{\Gamma_1^D(t)}$ at an edge site, $i = 1$, for a systems of varying size L . (a) Log plot of the finite-size excitation energies, showing a bond-breaking YY-chain energy gap, $\Delta_\delta = 2\delta$, and the zero-mode gap, $\Delta_L = E_1 - E_{GS}$, as functions of system size L . We note that Δ_δ is independent of system size L , and that Δ_L is repeated in the entire spectrum. (b) The inset shows the bare energy of the lowest four levels for various system sizes L . The two characteristic frequencies in the temporal evolution of $\overline{\Gamma_1^D(t)}$ correspond to the transitions $E_{GS} \leftrightarrow E_3$ and $E_1 \leftrightarrow E_2$. (c, d) The long-time evolution of the edge autocorrelation function (8) for chains of length $L = 8$ and $L = 10$, respectively. The characteristic frequency $\propto \Delta_\delta$ does not change with L . The revivals of the oscillations correspond to a beat frequency $f_{beat} \propto \Delta_L$, which is, however, directly dependent on the zero mode gap, Δ_L , which in turn depends on L . The expected beat frequencies calculated directly from the spectral gaps are $T_{beat}^{L=8} = 259$ and $T_{beat}^{L=10} = 673$, which is in good agreement with the observed dynamics.

owing to the fact that σ_1^x does not couple the different zero mode eigenstates. We find that the spin precession frequency of σ_1^x and σ_1^z is independent of the chosen initial state, since it explicitly depends on global gaps Δ_δ in the spectra. These correspond to the gap within the edge unit cell, given by the perturbation $\delta \hat{S}_i^y \hat{S}_{i+1}^y$. Since σ_1^x toggles between levels within the unit cell split by δ , but not between zero mode eigenstates, it corresponds only to the oscillation frequency from the gap Δ_δ . The operator σ_1^z on the other hand, toggles between *both* zero modes and unit cell energy levels. The decoherence time now relates directly to the toggling between different zero modes, corresponding to gaps Δ_L given by the commutation of the zero modes and the Hamiltonian. This correspondence is shown in Fig. 4, where the autocorrelation is evaluated for longer times. Away from the Kitaev point θ_{KP} the global gaps are no longer present, so the oscillations decay quickly in both the TLL and XY phase.

Figure 5 shows that the persistent edge oscillations are entirely absent in the other parts of the phase diagram, where zero modes are not present. In these cases there are no global degeneracies in the Hamiltonian, and oscillations at the edges simply decay in the same manner as for spins in the bulk, as seen from Fig. 5. Simulations show that the decoherence becomes more profound, meaning that the system is fully decohered for a longer time without signs of revival, as the

systems grow in size. We stress that the edges are still interacting with the bulk in this MEM phase, which becomes apparent from the fact that the coherence times increase with L (not shown here). This means that we cannot think of the edges and bulk as two completely separate systems described in terms of a tensor product between them. However, observables like $\Gamma_1^x(t)$ may still have trivial behavior if they fully commute with the Hamiltonian, as seen in Fig. 3.

From the above results, we conclude that the autocorrelation function can reveal a clear signature for the existence of zero modes in the Hamiltonian, providing the correct spins are measured. The oscillations are visible only for the edges and not in the bulk since the bulk spins generally decohere fast [49]. A handy explanation is offered in the limit $\delta \gg 1$ where we notice that applying a local spin- z at the edge adds the energy cost of breaking (or creating) exactly one antiferromagnetic bond: The operator $\hat{\sigma}_1^z$, which acts as a spin-flip operator on a local spin $-y$ state at the edge, will necessarily break *or* create exactly one bond, connecting states separated in energy by the gap $\Delta_\delta = \delta$. These gaps are present throughout the spectrum and result in a large set of coherent terms in the autocorrelation function (15), giving a significant contribution for long times. For $\hat{\sigma}_i^z$, acting on a bulk state $L > i > 1$, a spin flip is instead associated with either simultaneous creation *and* destruction of one bond (or simultaneous creation

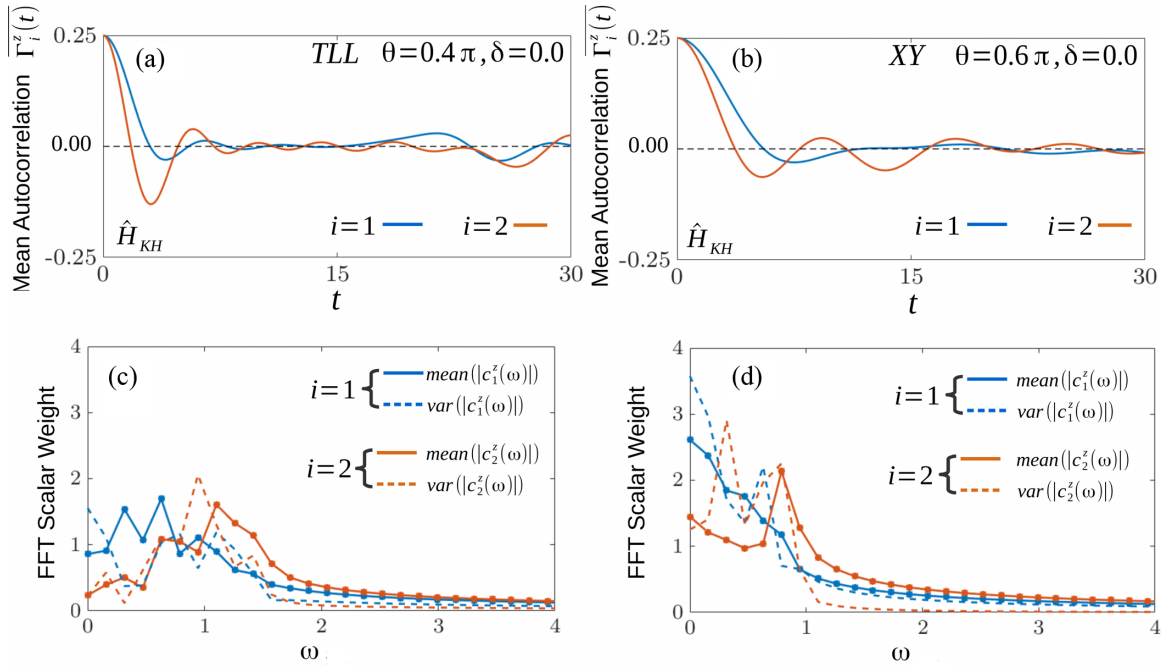


FIG. 5. Same as Fig. 3, but for the TLL phase (a), (c) and the XY phase (b), (d). Each of these phases displays a broad distribution of frequencies, with high variance both in the bulk and at the edge. This is manifested in the rapid decay of the real-time oscillations in (a) and (b). This is in strong contrast to the edge oscillations in the MEM phase, providing a clear signal for the onset of Majorana edge modes at $\theta = 0.5\pi, \delta > 0$.

or destruction of *two* bonds) and will thus connect states with energy differences smaller than the gap. This gives rise to a set of low frequencies contributing to the temporal evolution of the bulk spin, causing an effective decay of the oscillations. In the limit of small δ , this discrepancy between bulk and edge is reduced since Δ_δ is then of the same order as other, small gaps in the spectrum. From the dynamical simulations, we find that the number of dominating frequencies for the first bulk spin corresponds to $N_{\text{peaks}} = L - 2$ which means that for successively larger systems, the oscillations in real time will be washed out for this site. The high relative variance for the bulk spins, see Fig. 3 furthermore shows that the exact dynamics here depend heavily on the input state. Directly at the Kitaev point, the number of dominating frequencies corresponds to the system size L ($N_{\text{peaks}} = L/2$). The frequencies are independent of the site index and input state, whereas their relative weights depend on the site index. This explains why no coherent oscillations are seen directly at the Kitaev point.

In the limit of long-time spin precession for the MEM phase we observe decay and revival of the oscillation at the edge, resulting in a beating pattern. The beating pattern, with period T_{beat}^L , observed in Fig. 4 is a finite-size effect directly related to the revival of decohering spins, which was noted for the pure Ising model in Refs. [50,61], where the revival time scaled with system size. The envelope function in Eq. (22) is given by the same function as for the spin σ_1^y , which has some important consequences. We know that the decoherence and revival times of the autocorrelation function here are related to the correction term \mathcal{C} [50], so these properties are therefore identical for σ_1^y and σ_1^z . The revival time scales with the few-body gap $\sim 1/\Delta_L$, as evident in Fig. 4. As noted before, Δ_L is identical for $\hat{H}_\delta^{\text{Ising}}$ and $\hat{H}_\delta^{\text{inter}}$. We have shown that the

long-time properties of these two systems can be mapped onto those of an effective Ising model with two-site unit cells. The complete revival and resulting beating pattern in the autocorrelation plots of Fig. 4, scaling with $T_{\text{beat}}^L \propto 1/\Delta_L$, is therefore not surprising.

V. QUANTUM SIMULATION WITH TRAPPED IONS

For a possible quantum simulation of the MEM phase, we here sketch a setup with ions trapped utilizing radio frequency (RF) fields [63–65]. Experiments with such systems typically realize effective Ising, XY, or XYZ spin-spin interactions, and may be supplemented with global transverse fields terms [66,67]. These setups have been used in a large number of studies, for example simulation of quantum magnets [68] entanglement propagation [37], and variations on the quantum Ising spin chains [25,69,70], along with more general quantum computing implementations [71,72]. Whereas most quantum simulation experiments with trapped ions use a linear configuration we will consider a geometry where the trapping frequencies perpendicular to the tap axis are very different. For suitable parameters this ensures that the ions form a planar zig-zag structure as shown in Fig. 6. The use of a zig-zag configuration allows for the direction and magnitude of a laser field to control the size and sign of effective interactions between different rungs of the zig-zag spin ladder [74] and we will exploit this below. Furthermore, we assume that every third ion in our setup is selectively hidden, requiring individual addressing of ions [75], so that they do not participate in the simulation. The resulting pattern is sketched in Fig. 6. To ensure a uniform distance between ions, we consider only the central part of a crystal containing $N \sim 100$ ions and

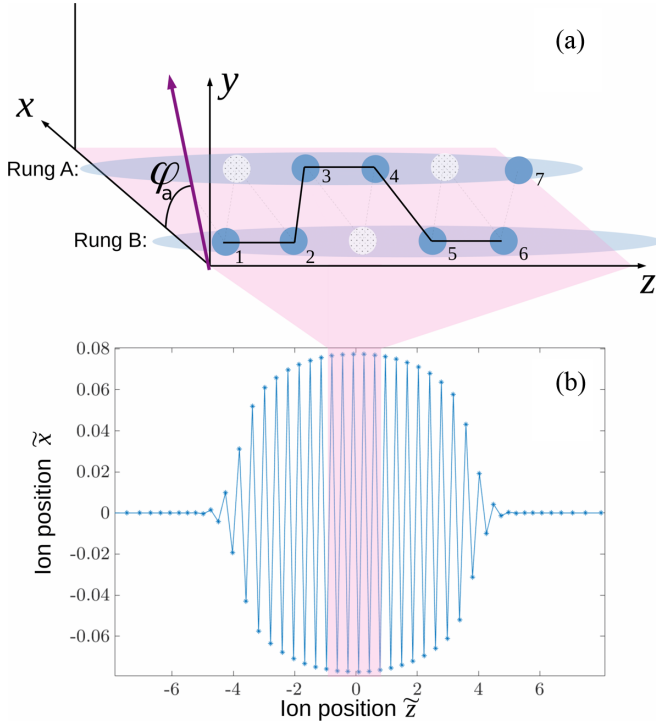


FIG. 6. (a) Sketch of the zig-zag configuration of ions in an RF trapping potential. The direction of optical beams is given by $\varphi_a \sim \pi/2$ in the xy plane. Every third ion is hidden, as indicated by the white circles, producing the effective order of interacting two-level systems denoted by the numerals. (b) Numerically simulated equilibrium positions of $N = 70$ ions for the considered trap parameters $\omega_x = 18.75\omega_z$ and $\omega_y = 125\omega_z$. We assume that all ions outside the central region are hidden, so that the distance between different rungs is roughly uniform for the participating ions. Alternatively, a similar uniform spacing can be achieved by shaping the trapping potential [73].

assume that all other ions do not participate in the simulation, e.g., because they have been optically pumped to a different internal level [75]; see Fig. 6. Alternatively, a more uniform distribution could also be obtained by carefully adjusting the local trapping potential [73].

For convenience, we first employ a simple rotation on the Hamiltonian in Eq. (1) so that

$$X \rightarrow Z_{\text{sim}} \quad Y \rightarrow X_{\text{sim}} \quad Z \rightarrow Y_{\text{sim}}, \quad (23)$$

where the subscript “sim” denotes the axes of the simulated Hamiltonian. We aim to realize the Hamiltonian

$$\begin{aligned} \hat{H} = & \sum_{j'=1}^{L/2} V_{j'}^{\text{a,odd}} \hat{S}_{2j'-1}^z \hat{S}_{2j'}^z + \sum_{j'=1}^{L/2} V_{j'}^{\text{b,odd}} \hat{S}_{2j'-1}^x \hat{S}_{2j'}^x \\ & + \sum_{j'=1}^{L/2} V_{j'}^{\text{b,even}} \hat{S}_{2j'}^x \hat{S}_{2j'+1}^x + \text{H.c.} \end{aligned} \quad (24)$$

with the purpose of simulating the effective Hamiltonian $\hat{H}_\delta^{\text{Ising}} = \hat{H}_{\text{KH}}(\theta = \pi/2) + \hat{V}_\delta^{\text{Ising}}$ from the previous section. We note that the indices j' correspond to the effective indices in the simulated Hamiltonian, which correspond to the *active* (not hidden) ions inside the ion trap, as shown in Fig. 6(a).

For the choice $V_{j'}^{\text{a,odd}} = V_{j'}^{\text{b,odd}} = V_{j'}^{\text{b,even}}/2$ the Hamiltonian \hat{H}_{sim} reduces to $\hat{H}_{\delta_{\text{eff}}}^{\text{Ising}}$ with $K = 1$ and $\delta_{\text{eff}} = 1$, assuming the couplings $V_{j'}^{\text{a,odd}}$, $V_{j'}^{\text{b,odd}}$ and $V_{j'}^{\text{b,even}}$ are uniform.

As we discuss below a major challenge is to remove additional interactions induced by the coupling mechanism corresponding to next-nearest neighbor (or higher) interactions in each of the effective ZZ and XX interactions. The residual interactions will cause decoherence and need to be reduced enough for the beating mechanism to be observed at different system sizes L . We find that a suitable parameter regime to aim for is $\delta_{\text{eff}} \sim 1$.

The signature of the MEM phase of $\hat{H}_\delta^{\text{Ising}}$ requires the edge spin to be initially prepared in an eigenstate of \hat{S}_1^y . This can be achieved by optical pumping and subsequent $\pm\pi/2$ rotations around the x axis [76,77]. The remaining spins can be prepared into any mixed state, but to be consistent with the previous sections we here assume their initial states to also be eigenstates of \hat{S}_i^y . With the initial spin-state s_1^y known, the autocorrelation function $\Gamma_i^y(t)$ in Eq. (8) can be evaluated by measuring the spin along y at a later time t .

We now proceed to discuss the realization of the two different interactions in \hat{H}_{sim} , starting with the ZZ interaction. For a detailed derivation and discussion of parameters of the ion-trap simulation, see the Supplemental Materials [57] Sec. VII.

A. Simulating ZZ and XX interactions

For the ZZ interaction we consider a two-photon Λ scheme where the lasers coupling two stable ground levels $|\uparrow\rangle$ $|\downarrow\rangle$ to an excited state are far-off resonant with the dipole allowed transition and the detuning is given by \mathcal{D} which is much larger than the spontaneous decay rate of the system. In line with Refs. [66,74] we employ a pair of laser fields with effective Rabi frequencies $\Omega_{1,\zeta}$ and $\Omega_{2,\zeta}$ for $\zeta = \uparrow, \downarrow$ coupling the ground levels ζ to the excited state. The effective Raman wave vector of the two fields is given by $\vec{k}_l^a = \vec{k}^1 - \vec{k}^2 = k_l^a \{\cos \varphi_a, \sin \varphi_a, 0\}$, and can be tuned via alignment of the lasers. The laser beatnote $\omega_l^a = \omega_1 - \omega_2$ of the fields is chosen close to the ions' collective vibrational motion in the transversal direction y , with mode energies ω_p^y , and far-off resonance with the vibrational modes in the zig-zag plane with mode energies ω_p^{xz} . The transverse vibrational modes act as mediators of an effective spin-spin interaction of the canonically transformed Hamiltonian [66], and by carefully choosing the detunings and alignments of the laser fields a nonisotropic effective ZZ interaction with tunable strength and range can be realized [74]:

$$\tilde{V}_{ij}^a = \sum_{ij} V_{ij}^a \hat{\sigma}_i^z \hat{\sigma}_j^z. \quad (25)$$

The overall strength of the interaction is controlled by the magnitude and direction of the laser fields, affording some freedom in choosing the parameters in our effective Hamiltonian. Crucially, the factor V_{ij}^a is dependent the alignment of the field and the relative equilibrium positions \vec{r}_{ij}^0 of the interacting ions, so that the nonhomogeneity of the interaction

can be tailored via the fields:

$$V_{ij}^a \propto -\Omega_a^2 (\sin \varphi_a)^2 \cos [k_l^a (x_j - x_i) \cos \varphi_a + (y_j - y_i) \sin \varphi_a]. \quad (26)$$

The effective two-photon Rabi frequency is given by $\Omega_a = (\Omega_{1,\downarrow} \Omega_{2,\downarrow}^* + \Omega_{1,\uparrow} \Omega_{2,\uparrow}^*)/2D$.

For the zig-zag configuration of the ions, it is convenient to choose \vec{k}_l^a in the xy plane, i.e., perpendicular to the direction of the rungs, as shown in Fig. 6 so that

$$\text{Same rung: } \cos(\vec{k}_l^a \vec{r}_{ij}^0) = 1;$$

$$\text{Different rungs: } \cos(\vec{k}_l^a \vec{r}_{ij}^0) = \cos[(x_i - x_{i+1}) \cos \varphi_a].$$

By choosing the angle φ_a we can now eliminate the interaction between *different* rungs, even when the optical wavelength is small relative to the mutual ion distances [74].

We numerically calculate the equilibrium configuration of the ion trap with $N = 70$ to find the ions' positions and their transverse vibrational eigenmodes. We employ these quantities to evaluate the full expression for the effective interaction given in the Supplemental Materials [57] Sec. VII. Choosing the detunings of the fields, relative to the vibrational mode energies along y such that $(\omega_p^y - \omega_l^a)/\omega_p^y \sim 0.05$, we find that the typical distance dependence of the interaction strength becomes $\sim 1/|i - j|^R$ with $R \sim 3$. Since this falls off quickly with the distance, the interaction will be dominated by NN interactions [78]. We see from Fig. 6(a) that by hiding every third ion, we can map the same rung NN interaction to odd indices in the effective system whereas different rungs corresponds to NN interactions starting on even indices:

$$\text{Different rung: } \tilde{V}_{i,i+1}^a \rightarrow V_{2i',2i'+1}^a,$$

$$\text{Same rung: } \tilde{V}_{i,i+2}^a \rightarrow V_{2i'-1,2i'}^a \quad (27)$$

for the effective indices i' of the active ions.

For the effective XX interaction we need to drive a transition between two internal levels. This can either be done directly or as a two-photon Raman transition. The effective spin coupling is implemented via the vibrational sidebands of the transition [36]. The angular frequencies of the driving are given by $\omega_1^b = \omega^b - \omega_l^b$ and $\omega_2^b = \omega^b + \omega_l^b$. Here ω^b is the transition frequency between the considered internal levels of the ions. The detuning ω_l^b is roughly matched to the transverse trapping frequency ω_y so that $\omega_l^b \approx \omega_y$. We aim to virtually excite the vibrational sidebands, and we employ the sideband detuning $\gamma^b = \omega_l^b - \omega_y$. The sideband detuning is chosen to be positive, so that the ω_l^b lies above the highest vibrational mode along y (out of plane), which is the center of mass mode $\omega_{c.o.m.}$. We employ the same vibrational branch as for ZZ, but we assume there are no interference effects between the processes implementing ZZ and XX. This can be achieved by ensuring that the frequencies are incommensurate. The virtual phonon exchange between ions induces an effective interaction

$$\tilde{V}_{ij}^b = |\Omega_b|^2 \frac{\hbar |k_l^b|^2}{4} \sum_p \frac{M_{i,p} M_{j,p}}{(\omega_p^b)^2 - \omega_p^2}, \quad (28)$$

where the vibrational mode eigenvectors M_p and mode energies ω_p are for the strongly confined direction y [79].

We again employ the calculated vibrational modes and ion positions to explicitly calculate the effective interaction. The overall strength of the XX interaction can be controlled by the effective Rabi frequency Ω_b [36]. Choosing the detuning $(\omega_p^y - \omega_l^b)/\omega_p^y \sim 0.05$, we may realize approximate interactions $\sim 1/|i - j|^R$ with $R \sim 3$ for the XX interaction, so that residual terms are of similar order as for ZZ. The detuning is chosen to be different than that for the ZZ interaction, but on the same order of magnitude. Since there is no angular factor in Eq. (28) the effective interaction connects both sites within the same rung and sites between rungs.

Putting everything together, we obtain for the zig-zag indices i, j :

$$\begin{aligned} \hat{H}_{\text{sim}} = & \sum_i^L (\tilde{V}_{i,i+2}^a \hat{S}_i^z \hat{S}_{i+2}^z + \tilde{V}_{i,i+2}^b \hat{S}_i^x \hat{S}_{i+2}^x) + \sum_i^L \tilde{V}_{i,i+1}^b \hat{S}_i^x \hat{S}_{i+1}^x \\ & + \sum_{|i-j|>2}^L (\tilde{R}_{ij}^a \hat{S}_i^z \hat{S}_j^z + \tilde{R}_{ij}^b \hat{S}_i^x \hat{S}_j^x) + \text{H.c.} \end{aligned} \quad (29)$$

We now use the mapping in Eq. (27) to transform into the indices i', j' for the *active* ions:

$$\begin{aligned} \hat{H}_{\text{sim}} = & \sum_{i'}^{L/2} (V_{2i'-1,2i'}^a \hat{S}_{2i'-1}^z \hat{S}_{2i'}^z + V_{2i'-1,2i'}^b \hat{S}_{2i'-1}^x \hat{S}_{2i'}^x) \\ & + \sum_{i'}^{L/2} V_{2i',2i'+1}^b \hat{S}_{2i'}^x \hat{S}_{2i'+1}^x \\ & + \sum_{|i'-j'|>1}^L (R_{i'j'}^a \hat{S}_{i'}^z \hat{S}_{j'}^z + R_{i'j'}^b \hat{S}_{i'}^x \hat{S}_{j'}^x) + \text{H.c.} \end{aligned} \quad (30)$$

This form of the Hamiltonian agrees with the desired model in Eq. (24) apart from the residuals in the last line. According to the arguments above these residuals can be rather small. Furthermore, for a translationally invariant system, the desired coefficients will be identical between units cells as desired and can be adjusted to the desired values ratio to realize the MEM phase of the Kitaev-Heisenberg model.

For a real ion trap, the parameters can suffer from numerous imperfections. In particular, for a standard ion trap, the density will be higher near the center of the trap and the ions will not be equidistant, as shown in Fig. 6. In principle this can be overcome by carefully designing the trapping potential [80,81], but below we explore the limitations imposed by operating in a standard ion trap with harmonic confinement.

To investigate the imperfections in a real ion trap we consider the situation depicted in Fig. 6, consisting of 70 trapped ions, see the Supplemental Materials [57] Sec. VII for further details. To evaluate the role of imperfections the coefficients V_{ij}^a, V_{ij}^b and residuals are evaluated for the numerically calculated ion positions and eigenstates. We specifically do this by first fixing $|k_l^a|, |k_l^b|$ and then the angle φ_a so that different rung interactions disappear for ZZ, and proceed to choose the exact detunings for all fields. We can then finally match the Rabi frequencies Ω_a and Ω_b so that $V_{2i',2i'+1}^a \sim V_{2i',2i'+1}^b \sim V_{2i',2i'+1}^b/2$, mapping the simulated Hamiltonian (30) onto $\hat{H}_\delta^{\text{Ising}} = \hat{H}_{\text{KH}}(\theta = \pi/2) + \hat{V}_\delta^{\text{Ising}}$ with $\delta_{\text{eff}} \sim 1$, with additional residual terms. Using the numerically coupling co-

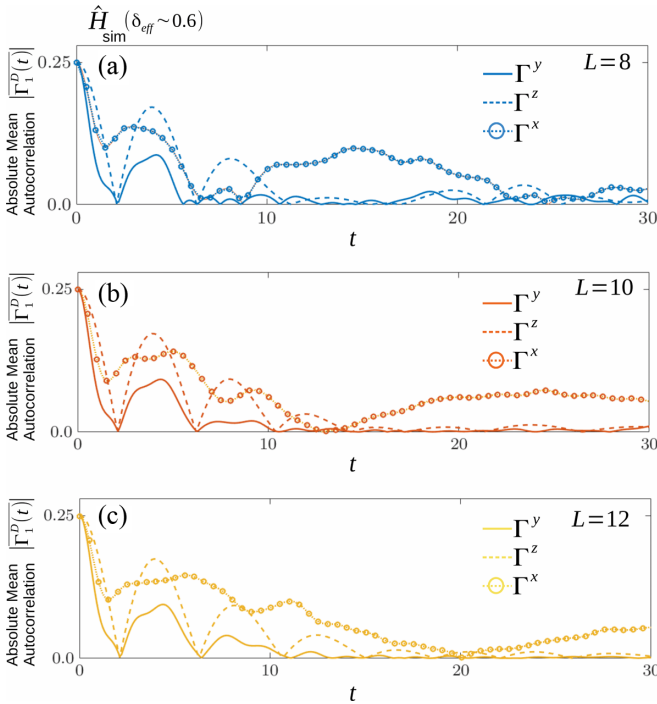


FIG. 7. Time evolution of the absolute mean autocorrelation $|\overline{\Gamma_1^D(t)}|$ of an the at an edge site, $i = 1$, from a numerical simulation of the ion trap Hamiltonian in Eq. (30). For the parameters considered in the Supplemental Materials [57] Sec. VII, we realize $K = 1$, $\delta_{\text{eff}} \sim 0.61$ with residuals $O(10^{-1})$. In principle other values of δ_{eff} can be simulated by adjusting the setup. The set of initial states are chosen as pure eigenstates to the operator \hat{S}_i^D . Panels (a)–(c) indicate that by increasing the number of active ions in the simulation, one can observe a heavily damped beating pattern in $|\overline{\Gamma_1^D(t)}|$, corresponding to the undamped beating pattern observed for $|\overline{\Gamma_1^D(t)}|$ in Fig. 3(a) (for the idealized Hamiltonian). Note that the simulated Hamiltonian is rotated relative to the idealized Hamiltonians via Eq. (23), so that the oscillation for $|\overline{\Gamma_1^D(t)}|$ indeed corresponds to the oscillation for $|\overline{\Gamma_1^X(t)}|$ in Fig. 3(a). We see that $|\overline{\Gamma_1^D(t)}|$ exhibits revivals of the long-time coherence scaling with L . This is due to the presence of a strong zero mode in the Hamiltonian. The coherence time t_c^z of the oscillation in $|\overline{\Gamma_1^D(t)}|$, on the other hand, is more independent of system size since it does not correspond to a zero mode. Its decoherence is explained by the residual terms in the quantum simulation and gives an overall estimate of the influence of impurities in the simulation. The oscillation of $|\overline{\Gamma_1^D(t)}|$ should exhibit a beating pattern in the limit of an idealized Hamiltonian, but decoheres on the same timescale as $|\overline{\Gamma_1^D(t)}|$. There is however an indication of the first node in the beating in $|\overline{\Gamma_1^D(t)}|$ for $L = 8$, which occurs before the system has fully decohered. This is seen from the node in $|\overline{\Gamma_1^D(t)}|$ at $t \approx 6$, which is pushed towards longer times for larger system sizes L .

efficient we can then proceed to evaluate the dynamics in the MEM phase corresponding to the time evolution in Fig. 4.

The results of a numerical simulation, performed for ~ 40 sampled initial states, of the ion trap are shown in Fig. 7. For the simulated setup the residual terms, the largest of which correspond to $\sim 10\%$ of V^a and V^b , clearly have a large effect on the results. The beating pattern visible for the idealized Hamiltonian in Eq. (24) is hard to observe due to the rapid decay of oscillations in the autocorrelations. We can however

see the size-dependent revivals for the long-time coherent spin along one of the axes, here along x [Note that when comparing to the idealized Hamiltonian we use the rotation (23)]. In Fig. 4, showing the dynamics of the idealized Hamiltonian, we further had two precessing spin components which were enveloped by a long-time beating.

Here we also saw that the decoherence of one of the precessing spin components (z) was enveloped by the long-time coherent autocorrelation function for the y -component, while the other precessing spin component (x), evolves more independently from the long-time coherent spin. This is behavior is somewhat visible also in the ion-trap simulation when comparing Figs. 7(a) and 7(b). We see that the oscillation of $|\overline{\Gamma_1^Z(t)}|$, which does not correspond to a zero mode, is less dependent on system size than the other spins. We conclude this by noticing that the oscillation of $|\overline{\Gamma_1^Z(t)}|$ is not suppressed in the region around the first node in $|\overline{\Gamma_1^X(t)}|$ for $L = 8$. However, the amplitude of the oscillating $|\overline{\Gamma_1^Z(t)}|$ is suppressed in this region. For $L = 10$, the oscillation in $|\overline{\Gamma_1^Z(t)}|$ is instead suppressed at slightly later times. This is due to the longer coherence time of $|\overline{\Gamma_1^Z(t)}|$, which envelops the oscillation, as shown in Sec. IV C. It is, however, evident that the precession in $|\overline{\Gamma_1^Z(t)}|$ also suffers from the same type of decoherence as $|\overline{\Gamma_1^Z(t)}|$, since there is no visible revival for $|\overline{\Gamma_1^Z(t)}|$. This gives an estimate for the influence of the residual interactions in the simulated Hamiltonian, since $|\overline{\Gamma_1^Z(t)}|$ should not decohere in the limit of zero residuals. [Compare to the evolution of the corresponding $|\overline{\Gamma_1^Z(t)}|$ of the idealized Hamiltonian in Fig. 3(a).] The behavior of the spins away from the edge (not shown) is similar for the simulated Hamiltonian as for the idealized Hamiltonian, where the long-time coherence is seen also for s_2 but not for s_3 . There is also no spin precession away from the edge for either spin.

In the ideal case, the nodes in the beating and long-time coherent spin autocorrelation can be used as a direct measure of the finite-size Majorana gap $\Delta_L = E_1 - E_{GS}$, which effectively simulates finite-size scaling in the MEM phase. The residual interactions in the quantum simulation however cause the oscillation of the edge spin to decohere rapidly, generally before the first node. Furthermore, the residual interactions destroy the global degeneracy corresponding to the zero modes, so the gaps throughout the spectrum are no longer homogeneous for the simulated Hamiltonian. By making a more homogeneous distance between the ions and implementing additional fields at different detunings and angles into the quantum simulation, the residuals can be reduced. This would allow for the decoherence time t_c^z to be increased so that the first node, and subsequent revival of the oscillation in $|\overline{\Gamma_1^Z(t)}|$ can be observed for successively larger systems.

VI. CONCLUSIONS AND OUTLOOK

We have showcased dynamical features of the anisotropic Kitaev-Heisenberg Hamiltonian, particularly focusing on the behavior around the so-called Kitaev point at which a multi-degenerate set of Majorana modes appear. By perturbing the model with a nearest-neighbor term $\hat{S}^y \hat{S}^y$ on even sites, we

see that the model can be mapped directly onto the Majorana edge mode (MEM) phase of Kitaev's model for p -wave paired superconductors, with one additional degree of freedom per unit site. By perturbing with a uniform Ising term $\hat{S}^y \hat{S}^y$ between all sites, the additional degrees of freedom are lost but the system retains the Majorana edge modes.

Studying the direct time development of local spins under this Hamiltonian we show that the MEM phase of the latter system can be identified via the precession of edge-site spins, which oscillate with two dominant frequencies. This gives rise to a beating pattern corresponding to the finite-size energy gap between the semidegenerate Majorana edge-mode states. The precession frequency of the spin is set by the interaction within the outermost unit cell of the system, while the beating is enveloped by the long-time coherent spin dynamics, which depends on the system size L . This is analogous to the long-time coherence of edge spins in the Ising model, an effect caused by strong zero modes present in the system [49,50]. We show that zero modes affect the long-time coherence of the spins measured along two different axes in our model, while the dynamical evolution of a spin prepared along the third axis is independent of zero modes, and therefore independent of system size L . These characteristics are not present in other parts of the phase diagram, or for spins in the bulk.

Crucially, this method of studying the dynamical properties does not rely on the repeated and deterministic preparation of a *single* initial state. It instead requires only deterministic preparation of a single spin, while the remaining spins can be randomly distributed.

We sketch an ion-trap quantum simulation, in which the steady-state zig-zag configuration of harmonically confined ions is exploited to realize the MEM phase. We see that some finite-size scaling properties of the spin dynamics can be observed, even for a setup with relatively large residual interaction terms. If the residuals were to be further reduced, our setup and readout mechanism could realize a quantum simulation of an interesting numerical challenge: the finite-size scaling of collective Majorana edge modes.

ACKNOWLEDGMENTS

We would like to thank Lorenzo Campos Venuti for useful discussions. This work was supported by the Swedish Research Council under Grant No. 2018-00833, the U.S. Department of Energy under Grant No. DE-FG03-01ER45908, and the Danish National Research Foundation (Center of Excellence ‘‘Hy-Q,’’ Grant No. DNRF139).

-
- [1] J.-P. Xu, M.-X. Wang, Z. L. Liu, J.-F. Ge, X. Yang, C. Liu, Z. A. Xu, D. Guan, C. L. Gao, D. Qian *et al.*, *Phys. Rev. Lett.* **114**, 017001 (2015).
- [2] A. Stern, *Nature (London)* **464**, 187 (2010).
- [3] M. Leijnse and K. Flensberg, *Semicond. Sci. Technol.* **27**, 124003 (2012).
- [4] A. Y. Kitaev, *Phys. Usp.* **44**, 131 (2001).
- [5] G. Jackeli and G. Khaliullin, *Phys. Rev. Lett.* **102**, 017205 (2009).
- [6] C. E. Agrapides, J. van den Brink, and S. Nishimoto, *Sci. Rep.* **8**, 1815 (2018).
- [7] M. Greiter, V. Schnells, and R. Thomale, *Ann. Phys.* **351**, 1026 (2014).
- [8] Y. Kubota, H. Tanaka, T. Ono, Y. Narumi, and K. Kindo, *Phys. Rev. B* **91**, 094422 (2015).
- [9] A. Banerjee, C. Bridges, J.-Q. Yan, A. Aczel, L. Li, M. Stone, G. Granroth, M. Lumsden, Y. Yiu, J. Knolle *et al.*, *Nat. Mater.* **15**, 733 (2016).
- [10] Y. Singh and P. Gegenwart, *Phys. Rev. B* **82**, 064412 (2010).
- [11] F. Ye, S. Chi, H. Cao, B. C. Chakoumakos, J. A. Fernandez-Baca, R. Custelcean, T. F. Qi, O. B. Korneta, and G. Cao, *Phys. Rev. B* **85**, 180403(R) (2012).
- [12] J. Chaloupka, G. Jackeli, and G. Khaliullin, *Phys. Rev. Lett.* **105**, 027204 (2010).
- [13] H. Katsura, D. Schuricht, and M. Takahashi, *Phys. Rev. B* **92**, 115137 (2015).
- [14] W. Brzezicki, J. Dziarmaga, and A. M. Oleś, *Phys. Rev. B* **75**, 134415 (2007).
- [15] F. Serwane, G. Zürn, T. Lompe, T. Ottenstein, A. Wenz, and S. Jochim, *Science* **332**, 336 (2011).
- [16] I. Bloch, J. Dalibard, and W. Zwerger, *Rev. Mod. Phys.* **80**, 885 (2008).
- [17] S. Murmann, F. Deuretzbacher, G. Zürn, J. Bjerlin, S. M. Reimann, L. Santos, T. Lompe, and S. Jochim, *Phys. Rev. Lett.* **115**, 215301 (2015).
- [18] A. Wenz, G. Zürn, S. Murmann, I. Brouzos, T. Lompe, and S. Jochim, *Science* **342**, 457 (2013).
- [19] L. Bayha, M. Holten, R. Klemt, K. Subramanian, J. Bjerlin, S. Reimann, G. Bruun, P. Preiss, and S. Jochim, *Nature (London)* **587**, 583 (2020).
- [20] J. Bjerlin, S. M. Reimann, and G. M. Bruun, *Phys. Rev. Lett.* **116**, 155302 (2016).
- [21] C. Nayak, S. H. Simon, A. Stern, M. Freedman, and S. Das Sarma, *Rev. Mod. Phys.* **80**, 1083 (2008).
- [22] C. V. Kraus, M. Dalmonte, M. A. Baranov, A. M. Läuchli, and P. Zoller, *Phys. Rev. Lett.* **111**, 173004 (2013).
- [23] F. Iemini, L. Mazza, D. Rossini, R. Fazio, and S. Diehl, *Phys. Rev. Lett.* **115**, 156402 (2015).
- [24] N. Lang and H. P. Büchler, *Phys. Rev. B* **92**, 041118(R) (2015).
- [25] J. Zhang, G. Pagano, P. W. Hess, A. Kyprianidis, P. Becker, H. Kaplan, A. V. Gorshkov, Z.-X. Gong, and C. Monroe, *Nature (London)* **551**, 601 (2017).
- [26] L. Jiang, T. Kitagawa, J. Alicea, A. R. Akhmerov, D. Pekker, G. Refael, J. I. Cirac, E. Demler, M. D. Lukin, and P. Zoller, *Phys. Rev. Lett.* **106**, 220402 (2011).
- [27] J. D. Sau, B. I. Halperin, K. Flensberg, and S. Das Sarma, *Phys. Rev. B* **84**, 144509 (2011).
- [28] D. Xie, W. Gou, T. Xiao, B. Gadway, and B. Yan, *npj Quantum Inf.* **5**, 1 (2019).
- [29] A. S. Jermyn, R. S. K. Mong, J. Alicea, and P. Fendley, *Phys. Rev. B* **90**, 165106 (2014).
- [30] J. Bland, C. H. Greene, and B. Wehefritz-Kaufmann, *Phys. Rev. A* **103**, 023310 (2021).
- [31] F. Schäfer, T. Fukuhara, S. Sugawa, Y. Takasu, and Y. Takahashi, *Nat. Rev. Phys.* **2**, 411 (2020).

- [32] N. R. Cooper, J. Dalibard, and I. B. Spielman, *Rev. Mod. Phys.* **91**, 015005 (2019).
- [33] J. I. Cirac and P. Zoller, *Phys. Rev. Lett.* **74**, 4091 (1995).
- [34] D. Leibfried, B. DeMarco, V. Meyer, M. Rowe, A. Ben-Kish, J. Britton, W. M. Itano, B. Jelenković, C. Langer, T. Rosenband, and D. J. Wineland, *Phys. Rev. Lett.* **89**, 247901 (2002).
- [35] D. J. Wineland, C. Monroe, W. M. Itano, B. E. King, D. Leibfried, C. Myatt, and C. Wood, *Phys. Scr.* **1998**, 147 (1998).
- [36] A. Sørensen and K. Mølmer, *Phys. Rev. Lett.* **82**, 1971 (1999).
- [37] P. Jurcevic, B. P. Lanyon, P. Hauke, C. Hempel, P. Zoller, R. Blatt, and C. F. Roos, *Nature (London)* **511**, 202 (2014).
- [38] S. Boixo, S. V. Isakov, V. N. Smelyanskiy, R. Babbush, N. Ding, Z. Jiang, M. J. Bremner, J. M. Martinis, and H. Neven, *Nat. Phys.* **14**, 595 (2018).
- [39] G. Cohen, E. Gull, D. R. Reichman, and A. J. Millis, *Phys. Rev. Lett.* **115**, 266802 (2015).
- [40] S. R. White and A. E. Feiguin, *Phys. Rev. Lett.* **93**, 076401 (2004).
- [41] F. B. Anders and A. Schiller, *Phys. Rev. Lett.* **95**, 196801 (2005).
- [42] C. B. Dağ, L.-M. Duan, and K. Sun, *Phys. Rev. B* **101**, 104415 (2020).
- [43] F. J. Gómez-Ruiz, J. J. Mendoza-Arenas, F. J. Rodríguez, C. Tejedor, and L. Quiroga, *Phys. Rev. B* **93**, 035441 (2016).
- [44] F. J. Gómez-Ruiz, J. J. Mendoza-Arenas, F. J. Rodríguez, C. Tejedor, and L. Quiroga, *Phys. Rev. B* **97**, 235134 (2018).
- [45] J. J. Mendoza-Arenas, F. J. Gómez-Ruiz, F. J. Rodríguez, and L. Quiroga, *Sci. Rep.* **9**, 1 (2019).
- [46] H. Shen, P. Zhang, R. Fan, and H. Zhai, *Phys. Rev. B* **96**, 054503 (2017).
- [47] S. V. Syzranov, A. V. Gorshkov, and V. Galitski, *Phys. Rev. B* **97**, 161114(R) (2018).
- [48] M. Gessner, M. Ramm, H. Häffner, A. Buchleitner, and H.-P. Breuer, *Europhys. Lett.* **107**, 40005 (2014).
- [49] P. Fendley, *J. Phys. A: Math. Theor.* **49**, 30LT01 (2016).
- [50] J. Kemp, N. Y. Yao, C. R. Laumann, and P. Fendley, *J. Stat. Mech.* (2017) 063105.
- [51] Y. Wang, *Phys. Rev. E* **98**, 042128 (2018).
- [52] J. R. Colbert and P. A. Lee, *Phys. Rev. B* **89**, 140505(R) (2014).
- [53] G. Guennebaud, B. Jacob *et al.*, Eigen v3, <http://eigen.tuxfamily.org> (2010).
- [54] A. Kitaev, *Ann. Phys.* **321**, 2 (2006).
- [55] S. Mahdavifar, *Eur. Phys. J. B* **77**, 77 (2010).
- [56] E. Eriksson and H. Johannesson, *Phys. Rev. B* **79**, 224424 (2009).
- [57] See Supplemental Material at <http://link.aps.org/supplemental/10.1103/PhysRevB.106.035414> for additional details.
- [58] J. Alicea and P. Fendley, *Annu. Rev. Condens. Matter Phys.* **7**, 119 (2016).
- [59] S. Backens, A. Shnirman, Y. Makhlin, Y. Gefen, J. E. Mooij, and G. Schön, *Phys. Rev. B* **96**, 195402 (2017).
- [60] D. V. Else, P. Fendley, J. Kemp, and C. Nayak, *Phys. Rev. X* **7**, 041062 (2017).
- [61] P. Fendley, *J. Phys. A: Math. Theor.* **47**, 075001 (2014).
- [62] L. Campos Venuti, S. Yeshwanth, and S. Haas, *Phys. Rev. A* **87**, 032108 (2013).
- [63] H. Häffner, C. F. Roos, and R. Blatt, *Phys. Rep.* **469**, 155 (2008).
- [64] D. J. Wineland, C. Monroe, W. M. Itano, D. Leibfried, B. E. King, and D. M. Meekhof, *J. Res. Natl. Inst. Stand. Technol.* **103**, 259 (1998).
- [65] D. Leibfried, R. Blatt, C. Monroe, and D. Wineland, *Rev. Mod. Phys.* **75**, 281 (2003).
- [66] D. Porras and J. I. Cirac, *Phys. Rev. Lett.* **92**, 207901 (2004).
- [67] X.-L. Deng, D. Porras, and J. I. Cirac, *Phys. Rev. A* **72**, 063407 (2005).
- [68] A. Friedenauer, H. Schmitz, J. T. Glueckert, D. Porras, and T. Schätz, *Nat. Phys.* **4**, 757 (2008).
- [69] G. Pagano, A. Bapat, P. Becker, K. S. Collins, A. De, P. W. Hess, H. B. Kaplan, A. Kyprianidis, W. L. Tan, C. Baldwin *et al.*, *Proc. Natl. Acad. Sci. USA* **117**, 25396 (2020).
- [70] F. Liu, R. Lundgren, P. Titum, G. Pagano, J. Zhang, C. Monroe, and A. V. Gorshkov, *Phys. Rev. Lett.* **122**, 150601 (2019).
- [71] D. Kielpinski, C. Monroe, and D. J. Wineland, *Nature (London)* **417**, 709 (2002).
- [72] S. Gulde, M. Riebe, G. P. Lancaster, C. Becher, J. Eschner, H. Häffner, F. Schmidt-Kaler, I. L. Chuang, and R. Blatt, *Nature (London)* **421**, 48 (2003).
- [73] G.-D. Lin, S.-L. Zhu, R. Islam, K. Kim, M.-S. Chang, S. Korenblit, C. Monroe, and L.-M. Duan, *Europhys. Lett.* **86**, 60004 (2009).
- [74] A. Bermudez, J. Almeida, K. Ott, H. Kaufmann, S. Ulm, U. Poschinger, F. Schmidt-Kaler, A. Retzker, and M. Plenio, *New J. Phys.* **14**, 093042 (2012).
- [75] H. C. Nägerl, D. Leibfried, H. Rohde, G. Thalhammer, J. Eschner, F. Schmidt-Kaler, and R. Blatt, *Phys. Rev. A* **60**, 145 (1999).
- [76] S. Olmschenk, K. C. Younge, D. L. Moehring, D. N. Matsukevich, P. Maunz, and C. Monroe, *Phys. Rev. A* **76**, 052314 (2007).
- [77] D. Hayes, D. N. Matsukevich, P. Maunz, D. Hucul, Q. Quraishi, S. Olmschenk, W. Campbell, J. Mizrahi, C. Senko, and C. Monroe, *Phys. Rev. Lett.* **104**, 140501 (2010).
- [78] C. Monroe, W. C. Campbell, L.-M. Duan, Z.-X. Gong, A. V. Gorshkov, P. W. Hess, R. Islam, K. Kim, N. M. Linke, G. Pagano *et al.*, *Rev. Mod. Phys.* **93**, 025001 (2021).
- [79] K. Mølmer and A. Sørensen, *Phys. Rev. Lett.* **82**, 1835 (1999).
- [80] G. Pagano, P. W. Hess, H. B. Kaplan, W. L. Tan, P. Richerme, P. Becker, A. Kyprianidis, J. Zhang, E. Birkelbaw, M. R. Hernandez *et al.*, *Quantum Sci. Technol.* **4**, 014004 (2018).
- [81] M. Johanning, *Appl. Phys. B* **122**, 71 (2016).